



Ultra-low-loss on-chip resonators with sub-milliwatt parametric oscillation threshold

XINGCHEN JI,^{1,2} FELIPPE A. S. BARBOSA,^{2,3} SAMANTHA P. ROBERTS,² AVIK DUTT,^{1,2}  JAIME CARDENAS,^{2,4} YOSHITOMO OKAWACHI,⁵ ALEX BRYANT,⁶ ALEXANDER L. GAETA,⁵ AND MICHAL LIPSON^{2,*}

¹School of Electrical and Computer Engineering, Cornell University, Ithaca, New York 14853, USA

²Department of Electrical Engineering, Columbia University, New York, New York 10027, USA

³Current address: Instituto de Física, Universidade Estadual de Campinas, 13083-970 Campinas, SP, Brazil

⁴Current address: The Institute of Optics, University of Rochester, Rochester, New York 14627, USA

⁵Department of Applied Physics and Applied Mathematics, Columbia University, New York, New York 10027, USA

⁶School of Materials Science and Engineering, Georgia Institute of Technology, Atlanta, Georgia 30332, USA

*Corresponding author: ml3745@columbia.edu

Received 21 March 2017; revised 7 May 2017; accepted 8 May 2017 (Doc. ID 290891); published 6 June 2017

On-chip optical resonators have the promise of revolutionizing numerous fields, including metrology and sensing; however, their optical losses have always lagged behind those of their larger discrete resonator counterparts based on crystalline materials and silica microtoroids. Silicon nitride (Si_3N_4) ring resonators open up capabilities for frequency comb generation, optical clocks, and high-precision sensing on an integrated platform. However, simultaneously achieving a high quality factor (Q) and high confinement in Si_3N_4 (critical for nonlinear processes, for example) remains a challenge. Here we show that addressing surface roughness enables overcoming the loss limitations and achieving high-confinement on-chip ring resonators with Q of 37 million for a ring of 2.5 μm width and 67 million for a ring of 10 μm width. We show a clear systematic path for achieving these high Q s, and these techniques can also be used to reduce losses in other material platforms independent of geometry. Furthermore, we demonstrate optical parametric oscillation using the 2.5 μm wide ring with sub-milliwatt pump powers and extract the loss limited by the material absorption in our films to be 0.13 ± 0.05 dB/m, which corresponds to an absorption-limited Q of at least 170 million by comparing two resonators with different degrees of confinement. Our work provides a chip-scale platform for applications such as ultralow-power frequency comb generation, laser stabilization, and sideband-resolved optomechanics. © 2017 Optical Society of America

OCIS codes: (190.4380) Nonlinear optics, four-wave mixing; (220.4000) Microstructure fabrication; (240.5770) Roughness.

<https://doi.org/10.1364/OPTICA.4.000619>

1. INTRODUCTION

Low-propagation-loss silicon nitride (Si_3N_4) ring resonators are critical for a variety of photonic applications such as low-threshold frequency combs [1–5], optical clocks [6], and high-precision sensing [7–10]. High confinement is critical for tailoring the waveguide dispersion to achieve phase matching in nonlinear processes as well as for tighter bends in large-scale photonic systems. A microresonator's quality factor (Q) is extremely sensitive to losses. To date, ultrahigh Q s have been demonstrated only in discrete resonators based on platforms such as polished calcium fluoride (CaF_2) and magnesium fluoride (MgF_2) or silica microresonators [11–17] with typical cross-sectional mode field diameters much larger than the wavelength. Spencer *et al.* have recently demonstrated ring resonators with a high Q of up to 80 million using extremely thin (40 nm) Si_3N_4 films [18], which can be useful for narrowband filtering or building reference cavities for laser stabilization. However, they suffer from highly delocalized optical modes and millimeter-scale bending radii, making it challenging

to use these thin-film ring resonators for compact photonic routing or nonlinear applications requiring dispersion engineering. High confinement combined with low propagation loss is the key for efficient nonlinear optical processes. The highest intrinsic Q in high-confinement Si_3N_4 ring resonators reported to date is 17 million [19]. However, as Xuan *et al.* mention in their conclusion, a fabrication process that can predictably achieve an intrinsic Q larger than 10 million has not been achieved [19].

2. EFFECTS OF SURFACE ROUGHNESS ON HIGH-CONFINEMENT WAVEGUIDES

In this work, we show that surface roughness, rather than absorption from the bulk material, plays a major role in the loss limitations of Si_3N_4 , thereby enabling a path for achieving ultra-low-loss devices by addressing the surface quality. Absorption loss is mainly due to O–H bonds in SiO_2 , and N–H and Si–H bonds in Si_3N_4 [20]. Scattering loss comes primarily from the interaction of light

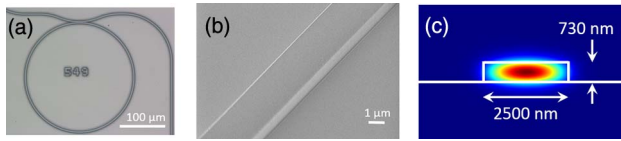


Fig. 1. Microscope images and mode simulation of the fabricated devices. (a) Top view optical microscope image of a 115 μm radius ring resonator. (b) Scanning electron microscopy image of a fabricated waveguide with smooth surfaces. (c) Mode simulation of a 730 nm tall and 2500 nm wide waveguide showing the mode is highly confined in the geometry we have chosen.

with the roughness of all the surfaces in a high-confinement waveguide. Mode simulations show that light propagating in the waveguide significantly interacts and scatters from both the patterned sidewalls and the top and bottom surfaces [see Fig. 1(c)]. Several groups have been working on reducing losses by improving the properties of the bulk material to achieve high Q [21–23]. However, to date, it has not been clear whether surface interactions or material absorption is the main source of the high loss in the integrated platform.

A. Sidewall Roughness Reduction

In order to reduce surface scattering from the sidewalls, we minimize the roughness introduced during the pattern transfer step of the processing by eliminating *in situ* polymer formation typical in the dry etching processes. Standard waveguide fabrication methods consist of patterning a masking layer, typically a photoresist or an electron-beam resist, and transferring this pattern into the photonic waveguide device layer using some form of plasma etching. Polymer formation is a common by-product of plasma etching [24,25]. *In situ* polymer deposition passivates the sidewalls and enables anisotropic etching, with vertical sidewalls desirable for fabrication of rectangular waveguides [26,27]. It also enables pattern transfer to thick waveguide device layers by enhancing the selectivity between the mask layer and the films. The polymer formed during this process, while critical for surface passivation and anisotropic etching, often leaves residue on the sidewalls, which introduces sidewall roughness. This roughness adds to the roughness introduced by the lithography itself [28,29]. Since the roughness is generally of the order of nanometers, it usually introduces negligible loss; however, it becomes significant in the high- Q regimes that we are aiming for here [20,30]. Trifluoromethane (CHF_3) and oxygen (O_2) gases are widely used as standard etchants in Si_3N_4 fabrication, and this etching chemistry is always accompanied by a polymer residue left on the sidewalls [31,32]. In order to reduce this polymer residue on sidewalls, we used a higher oxygen flow to remove *in situ* polymer formation, since oxygen reacts with the polymer residue to form carbon monoxide (CO) and carbon dioxide (CO_2). Oxygen also reacts with the photoresist, which is generally used in standard etching as the mask to transfer patterns. As a result, higher oxygen flow decreases the etching selectivity, degrading the ability to transfer patterns. To compensate for this effect, we use a silicon dioxide hard mask instead of a photoresist to maintain the ability to transfer waveguide patterns while eliminating *in situ* polymer formation on the sidewalls using a higher oxygen flow. Nitrogen is also added to increase the nitride selectivity over oxide [33,34].

In contrast to standard silicon-based waveguides with losses of the order of 1 dB/cm [35–37], where sidewall roughness plays the main role in inducing scattering loss, in ultra-low-loss Si_3N_4 , top surface roughness also plays a major role. Typically, roughness on the top and/or bottom surfaces has not attracted much attention due to the facts that sidewall roughness was quite significant and many of the previous studies relied on polished wafers or oxidized wafers from silicon photonics. Here we focus on reducing scattering loss from the top surface since the Si_3N_4 films are deposited using low-pressure chemical vapor deposition, and are not as inherently smooth as polished single-crystal wafers or oxidized wafers. Bottom surface roughness is not addressed here since its roughness, governed by thermal oxidation, is lower than the one governed by Si_3N_4 deposition.

B. Top Surface Roughness Reduction

In order to reduce scattering from the top surfaces, we reduce the roughness by chemical mechanical polishing (CMP) of the Si_3N_4 after deposition [as shown in Fig. 2(d)]. Atomic-force microscopy (AFM) scans before and after the polishing step are shown in Fig. 2. The root-mean-squared (RMS) roughness has decreased from 0.38 nm to 0.08 nm (AFM scans of different CMP Si_3N_4 films are shown in Supplement 1).

C. Lithography-Induced Roughness Reduction

To further decrease the loss, we apply multipass lithography to reduce line edge roughness known to contribute to scattering loss [38–40]. Electron-beam (e-beam) lithography, used extensively for patterning optical waveguides, creates a line edge roughness, which introduces extra roughness to the sidewalls. During e-beam lithography, any instability, such as beam current fluctuations, beam jitter, beam drift, stage position errors, and mechanical vibrations, can generate statistical errors, which result in extra line edge roughness in the patterns, which will add roughness to the sidewalls. The principle of multipass lithography [39,40] consists of exposing the same pattern multiple times at a lower current to reduce line edge roughness by averaging statistical errors.

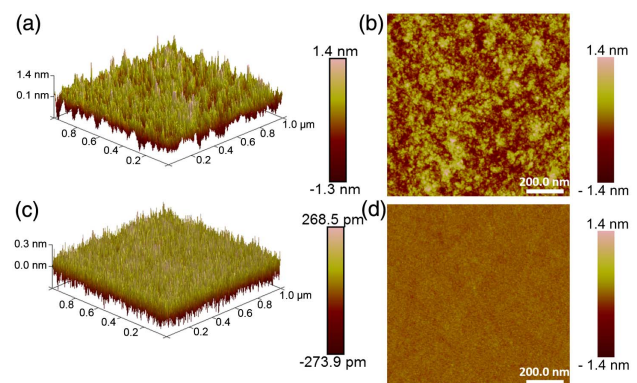


Fig. 2. AFM measurement of the top surface of Si_3N_4 . (a) 3D AFM scan of the top surface of Si_3N_4 before CMP with RMS roughness of 0.38 nm and correlation length of 29 nm. (b) 2D image of the top surface of Si_3N_4 before CMP and scaled to -1.4 to 1.4 nm with RMS roughness of 0.38 nm and correlation length of 29 nm. (c) 3D image of the top surface of Si_3N_4 after CMP with RMS roughness of 0.08 nm and correlation length of 8.76 nm. (d) 2D image of the top surface of Si_3N_4 after CMP and scaled to -1.4 to 1.4 nm with RMS roughness of 0.08 nm and correlation length of 8.76 nm. Note the different scale bars in (a) and (c).

3. OPTICAL MEASUREMENTS AND COMPARISONS

We measure an intrinsic Q of 37 ± 6 million in high-confinement Si_3N_4 ring resonators using the techniques described above. Mode splitting, commonly observed in ultrahigh- Q systems such as whispering-gallery-mode microresonators [41–43], is induced due to backscattering of light from fabrication imperfections or surface roughness. When Q is high and the mode is highly confined, extremely small defects or roughness can induce a visible splitting. We measured the transmission of four sets of fabricated ring resonators: (1) using the standard process we reported in Ref. [44] [Fig. 3(a)], (2) using our optimized etch process but without CMP and without multipass lithography [Fig. 3(b)], (3) using both the optimized etch recipe and CMP but without multipass lithography [Fig. 3(c)], and (4) using all the techniques, including the optimized etch recipe, surface smoothing technique, and multipass lithography [Fig. 3(d)]. All the rings have a radius of 115 μm , height of 730 nm, and width of 2500 nm, and are coupled to a waveguide of the same dimensions. The transmission spectra and linewidth of the resonator [full width at half-maximum (FWHM)] are measured using a laser scanning technique. We launch light from a tunable laser source, which is then transmitted through a fiber polarization controller and coupled into our device via an inverse nanotaper [45] using a lensed fiber. We collect the output of the ring resonator through another inverse nanotaper and an objective lens. We monitor the output on a high-speed InGaAs photodetector. The frequency of the laser is measured using a wavemeter with a precision of 0.1 pm and the laser detuning is calibrated by monitoring the fringes of a reference fiber-based Mach–Zehnder interferometer with a known free spectral range (FSR).

Figure 3 shows the measured transmission spectra of different ring resonators. We measured the ring resonators in the under-coupled regime so that the measured Q is close to their intrinsic Q .

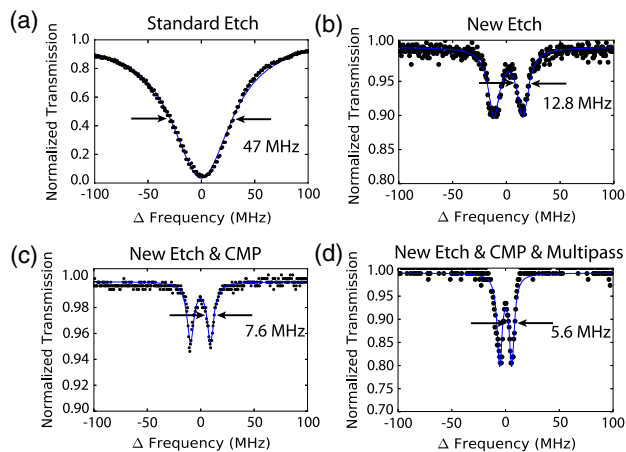


Fig. 3. Normalized transmission spectra of ring resonators fabricated using different processes. (a) Device fabricated using the standard process reported in Ref. [44] with a measured FWHM of 47 MHz. (b) Device fabricated using the optimized etch process, but without our new surface smoothing technique and multipass lithography with a measured FWHM of 12.8 MHz. (c) Device fabricated using both the optimized etch recipe and surface smoothing techniques, but without multipass lithography with a measured FWHM of 7.6 MHz. (d) Device fabricated using all the techniques including the optimized etch recipe, surface smoothing technique, and multipass lithography with a measured FWHM of 5.6 MHz.

The measured intrinsic Q s, estimated by measuring the transmission [46,47] for rings fabricated using processes (1)–(4) described above, are 5.6 ± 0.7 million, 16.2 ± 2.9 million, 28 ± 4.7 million, and 37 ± 6 million, which correspond to propagation losses of 5.2 ± 0.6 dB/m, 1.8 ± 0.3 dB/m, 1.1 ± 0.2 dB/m, and 0.8 ± 0.1 dB/m, respectively [48]. Note that these estimated propagation losses are the upper bounds on the losses in straight waveguides since in a ring the optical mode interacts more strongly with the sidewalls due to bending.

4. SUB-MILLIWATT OPTICAL PARAMETRIC OSCILLATION

In order to illustrate the importance of simultaneous high- Q and high-confinement ring resonators, we demonstrate a strong decrease in the threshold for optical parametric oscillation down to the sub-milliwatt level with decrease of optical losses. To determine the threshold for parametric oscillation, we measured the output power in the first generated four-wave-mixing sideband for different pump powers. Figure 4(a) shows the data for a device

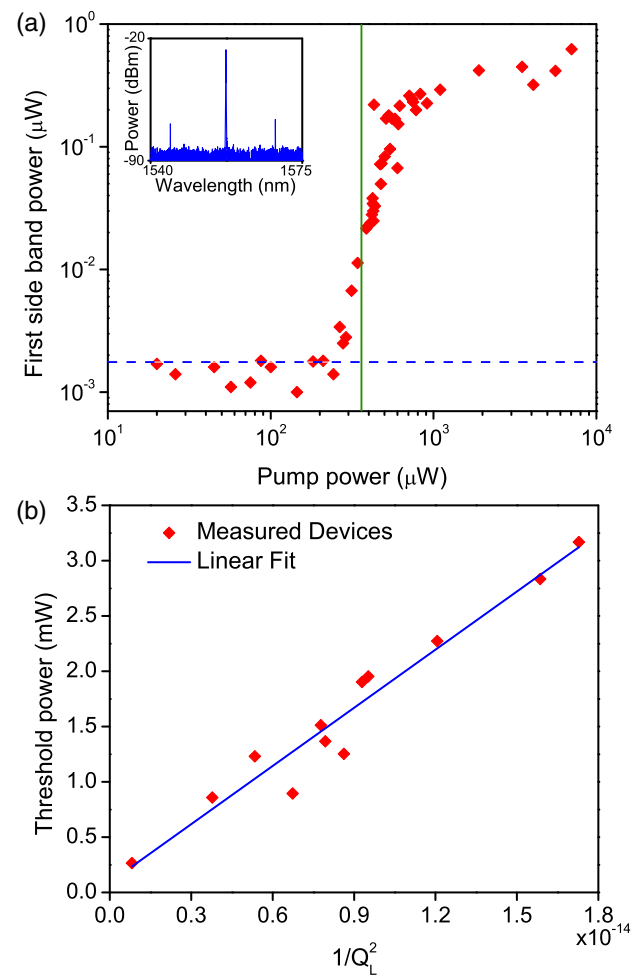


Fig. 4. Oscillation threshold decrease with decrease of losses. (a) Output power in the first generated mode as a function of pump power. In this device, parametric oscillation occurs for pump power of 330 ± 70 μW (indicated by the solid green vertical line). Note that the first band appears more than one FSR away from the pumped resonance. (b) Measured threshold power as a function of the loaded quality factor (Q_L) for microresonators with different fabrication processes. Threshold powers approximately follow the theoretically predicted trend of being inversely proportional to Q_L^2 .

pumped at the resonance near 1557 nm with a loaded Q of 35 million. The average threshold power is $330 \pm 70 \mu\text{W}$, comparable to the theoretically estimated threshold power of $206 \mu\text{W}$ using the expression [49,50]

$$P_{\text{th}} \approx 1.54 \left(\frac{\pi}{2} \right) \frac{Q_c}{2Q_L} \cdot \frac{n^2 V}{n_2 \lambda Q_L^2}, \quad (1)$$

where λ is the pump wavelength, n is the linear refractive index, n_2 is the nonlinear refractive index ($n_2 = 2.4 \times 10^{-19} \text{ m}^2/\text{W}$) [51], V is the resonator mode volume, and Q_c and Q_L are, respectively, the coupling and loaded quality factors of the resonators. This, to the best of our knowledge, is the lowest and the first sub-milliwatt power threshold parametric oscillation reported in planar nonlinear platforms [5,19,52–54] (Comparisons are shown in Supplement 1). In addition, this threshold power is close to the lowest threshold reported in ultrahigh- Q microresonators such as CaF_2 [55] and silica microtoroids [1]. We also measure and plot the thresholds for rings with various loaded quality factors in Fig. 4(b). The threshold powers follow the theoretically predicted trend of being inversely proportional to Q_L^2 .

5. FUNDAMENTAL LOSS LIMIT EXTRACTION

In order to extract the fundamental limit of achievable loss in silicon nitride waveguides, we compare the losses of two different structures, which have different mode interactions with the sidewalls. We estimate the bulk absorption limitation in our Si_3N_4 films to be $0.13 \pm 0.05 \text{ dB/m}$, which corresponds to an absorption-loss-limited Q of at least 170 million. We fabricated two devices with waveguide widths of $2.5 \mu\text{m}$ and $10 \mu\text{m}$ on the same wafer to ensure that the fabrication processes are identical. Both rings have the same height of 730 nm and they are coupled to a waveguide of the same dimensions ($730 \text{ nm} \times 2500 \text{ nm}$). The radius of the $2.5 \mu\text{m}$ ring is $115 \mu\text{m}$ and the radius of the $10 \mu\text{m}$ ring is $369 \mu\text{m}$ [mode simulations shown in Figs. 5(a) and 5(b)]. Figures 5(c) and 5(d) show, respectively, the measured transmission spectra for the $10 \mu\text{m}$ wide ring with in TE and TM polarizations. The measured intrinsic Q is 67 ± 7 million for the TE mode and 59 ± 12 million for the TM mode. At these ultrahigh Q , one is operating near the limits of Q , which can be reliably estimated by scanning a laser across a resonance. Hence, we corroborate these Q measurements by performing a cavity ring-down experiment for the TM mode [56–58,15,16]. As shown in Fig. 5(e), the measured lifetime is $25.6 \pm 1.3 \text{ ns}$, which corresponds to an intrinsic Q of 63 ± 3 million, consistent with our measurement of the Q , using a laser scanning technique. We estimate the fundamental loss limit given by the bulk absorption of Si_3N_4 in our films ($\alpha_{\text{total_absorption}}$) by comparing the losses for the two structures extracted from the transmission measurements ($\alpha_{\text{ring}} \sim 0.79 \pm 0.14 \text{ dB/m}$ and $\alpha_{\text{wide_ring}} \sim 0.43 \pm 0.046 \text{ dB/m}$) and considering the absorption of the rings with narrower and wider waveguides to, respectively, be

$$\alpha_{\text{ring}} = \alpha_{\text{total_absorption}} + \alpha_{\text{top_scatter}} + \alpha_{\text{bottom_scatter}} + \alpha_{\text{sidewalls_scatter}} \quad (2)$$

$$\alpha_{\text{wide_ring}} = \eta_1 \alpha_{\text{total_absorption}} + \eta_2 (\alpha_{\text{top_scatter}} + \alpha_{\text{bottom_scatter}}) + \eta_3 \alpha_{\text{sidewalls_scatter}} \quad (3)$$

η_1 , η_2 , and η_3 are factors that account for the interaction of the field with the waveguide core, the top and bottom surfaces, and

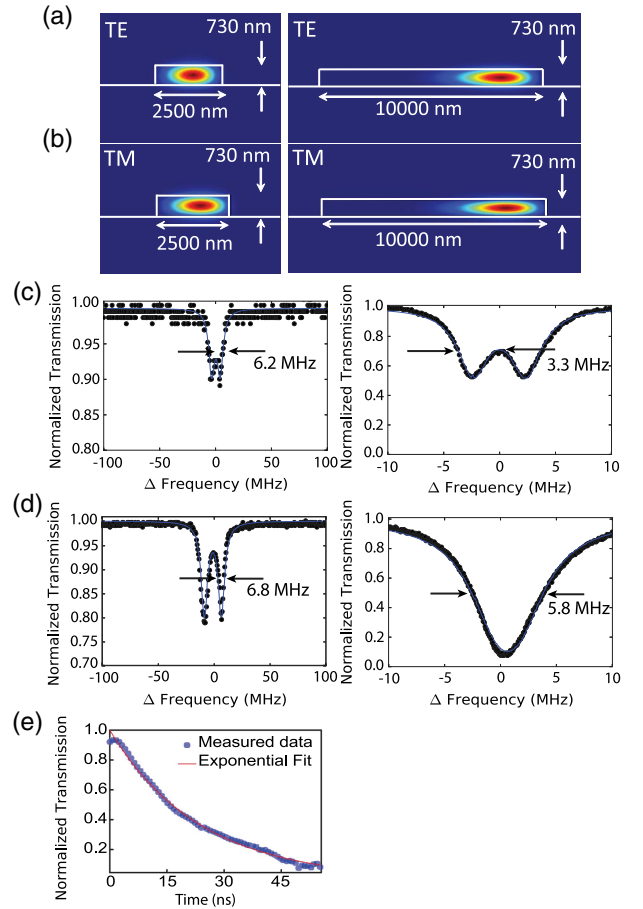


Fig. 5. Mode simulation and normalized transmission spectra for ring resonators with different interaction strengths with sidewalls. (a) TE mode profiles of waveguides that are $2.5 \mu\text{m}$ and $10 \mu\text{m}$ wide and 730 nm high using Si_3N_4 with a refractive index of 1.996 as the core material and SiO_2 with a refractive index of 1.446 as the cladding material. (The mode simulations have taken the bending radius into account). (b) Same as (a) but for TM. (c) Measured normalized TE transmission spectra of the ring resonator composed of the $2.5 \mu\text{m}$ wide waveguide (left) with a measured FWHM of 6.2 MHz and the measured spectra of the ring resonator composed of the $10 \mu\text{m}$ wide waveguide (right) with a measured FWHM of 3.3 MHz in TE polarization using the optimized fabrication process. (d) TM transmission spectra of the rings with the narrower (left) and the wider (right) waveguides with FWHMs of 6.8 MHz and 5.8 MHz , respectively. (e) Cavity ring-down measurement in TM mode. The measured lifetime extracted from the exponential fit is $25.6 \pm 1.3 \text{ ns}$.

the sidewalls, respectively, for the wider waveguides relative to the narrower waveguide [59] and are calculated using Finite element method simulations (performed with COMSOL) to be 1.010, 1.002, and 0.138, respectively. In our simulation, we have taken different bending radii into account. $\alpha_{\text{top_scatter}} \sim 0.007 \text{ dB/m}$ ($\pm 0.001 \text{ dB/m}$) and $\alpha_{\text{bottom_scatter}} \sim 0.24 \text{ dB/m}$ ($\pm 0.02 \text{ dB/m}$) are, respectively, the losses due to scattering at the top and bottom interfaces estimated from the Payne–Lacey model [60], which relates scattering loss to the surface’s RMS (σ) roughness and correlation length (L_c), which are both extracted from the AFM measurements (AFM scans of the bottom SiO_2 film are shown in Supplement 1). The scattering losses due to the sidewalls, $\alpha_{\text{sidewalls_scatter}}$, and the bulk loss are then extracted to be $0.41 \pm 0.05 \text{ dB/m}$ and

0.13 ± 0.05 dB/m, respectively. Note that we are assuming here that both sidewalls have the same loss as they experience the same e-beam lithography and plasma etching conditions, and the loss in the oxide cladding is negligible when compared with the loss in the Si_3N_4 due to the high degree of confinement.

6. CONCLUSIONS

In conclusion, we drastically and systematically reduced losses in high-confinement resonators by using methods for reducing roughness from waveguide interfaces. Moreover, we demonstrate optical parametric oscillation in an on-chip microresonator, with sub-milliwatt pump powers. We extract the absorption-limited Q of the ring resonator to be at least 170 million, which indicates that we are still limited by the scattering loss, thereby providing a path for achieving ultra-low-loss resonators simply via addressing the scattering loss. From our AFM measurements, one possible path for further decreasing these scattering losses is by addressing the roughness at the bottom cladding–core interface generated by the thermal oxidation process. Our work provides an on-chip platform for devices with performance that could be comparable to the performance achieved in discrete large devices.

Funding. Defense Advanced Research Projects Agency (DARPA) under the Microsystems Technology Office Direct On-Chip Digital Optical Synthesizer program (DODOS) (N66001-16-1-4052); Air Force Office of Scientific Research (AFOSR) (FA9550-15-1-0303); National Science Foundation (NSF) (ECCS-1542081).

Acknowledgment. The authors would like to thank Steven Miller and Aseema Mohanty and Dr. Carl B. Poitras for helpful discussions. The devices were partially fabricated at City University of New York Advanced Science Research Center and Cornell NanoScale Facility. X.J. is also grateful to the China Scholarship Council for financial support.

See [Supplement 1](#) for supporting content.

REFERENCES

- P. Del'Haye, A. Schliesser, O. Arcizet, T. Wilken, R. Holzwarth, and T. J. Kippenberg, "Optical frequency comb generation from a monolithic microresonator," *Nature* **450**, 1214–1217 (2007).
- J. S. Levy, A. Gondarenko, M. A. Foster, A. C. Turner-Foster, A. L. Gaeta, and M. Lipson, "CMOS-compatible multiple-wavelength oscillator for on-chip optical interconnects," *Nat. Photonics* **4**, 37–40 (2010).
- T. J. Kippenberg, R. Holzwarth, and S. A. Diddams, "Microresonator-based optical frequency combs," *Science* **332**, 555–559 (2011).
- A. A. Savchenkov, A. B. Matsko, V. S. Ilchenko, I. Solomatine, D. Seidel, and L. Maleki, "Tunable optical frequency comb with a crystalline whispering gallery mode resonator," *Phys. Rev. Lett.* **101**, 093902 (2008).
- L. Razzari, D. Duchesne, M. Ferrera, R. Morandotti, S. Chu, B. E. Little, and D. J. Moss, "CMOS-compatible integrated optical hyper-parametric oscillator," *Nat. Photonics* **4**, 41–45 (2010).
- S. B. Papp, K. Beha, P. Del'Haye, F. Quinlan, H. Lee, K. J. Vahala, and S. A. Diddams, "Microresonator frequency comb optical clock," *Optica* **1**, 10–14 (2014).
- T. Udem, R. Holzwarth, and T. W. Hänsch, "Optical frequency metrology," *Nature* **416**, 233–237 (2002).
- J. Zhu, S. K. Ozdemir, Y.-F. Xiao, L. Li, L. He, D.-R. Chen, and L. Yang, "On-chip single nanoparticle detection and sizing by mode splitting in an ultrahigh-Q microresonator," *Nat. Photonics* **4**, 46–49 (2010).
- S. A. Diddams, L. Hollberg, and V. Mbele, "Molecular fingerprinting with the resolved modes of a femtosecond laser frequency comb," *Nature* **445**, 627–630 (2007).
- T. Taniguchi, A. Hirowatari, T. Ikeda, M. Fukuyama, Y. Amemiya, A. Kuroda, and S. Yokoyama, "Detection of antibody–antigen reaction by silicon nitride slot-ring biosensors using protein G," *Opt. Commun.* **365**, 16–23 (2016).
- D. K. Armani, T. J. Kippenberg, S. M. Spillane, and K. J. Vahala, "Ultra-high-Q toroid microcavity on a chip," *Nature* **421**, 925–928 (2003).
- V. S. Ilchenko, A. A. Savchenkov, A. B. Matsko, and L. Maleki, "Nonlinear optics and crystalline whispering gallery mode cavities," *Phys. Rev. Lett.* **92**, 043903 (2004).
- I. S. Grudinin and L. Maleki, "Ultralow-threshold Raman lasing with CaF_2 resonators," *Opt. Lett.* **32**, 166–168 (2007).
- J. Hofer, A. Schliesser, and T. J. Kippenberg, "Cavity optomechanics with ultrahigh-Q crystalline microresonators," *Phys. Rev. A* **82**, 031804 (2010).
- I. S. Grudinin, V. S. Ilchenko, and L. Maleki, "Ultrahigh optical Q factors of crystalline resonators in the linear regime," *Phys. Rev. A* **74**, 063806 (2006).
- A. A. Savchenkov, A. B. Matsko, V. S. Ilchenko, and L. Maleki, "Optical resonators with ten million finesse," *Opt. Express* **15**, 6768–6773 (2007).
- H. Lee, T. Chen, J. Li, K. Y. Yang, S. Jeon, O. Painter, and K. J. Vahala, "Chemically etched ultrahigh-Q wedge-resonator on a silicon chip," *Nat. Photonics* **6**, 369–373 (2012).
- D. T. Spencer, J. F. Bauters, M. J. R. Heck, and J. E. Bowers, "Integrated waveguide coupled Si_3N_4 resonators in the ultrahigh-Q regime," *Optica* **1**, 153–157 (2014).
- Y. Xuan, Y. Liu, L. T. Varghese, A. J. Metcalf, X. Xue, P.-H. Wang, K. Han, J. A. Jaramillo-Villegas, A. A. Noman, C. Wang, S. Kim, M. Teng, Y. J. Lee, B. Niu, L. Fan, J. Wang, D. E. Leaird, A. M. Weiner, and M. Qi, "High-Q silicon nitride microresonators exhibiting low-power frequency comb initiation," *Optica* **3**, 1171–1180 (2016).
- M. J. Shaw, J. Guo, G. A. Vawter, S. Habermehl, and C. T. Sullivan, "Fabrication techniques for low-loss silicon nitride waveguides," *Proc. SPIE* **5720**, 109–118 (2005).
- W. M. A. Bik, R. N. H. Linssen, F. H. P. M. Habraken, W. F. van der Weg, and A. E. T. Kuiper, "Diffusion of hydrogen in low-pressure chemical vapor deposited silicon nitride films," *Appl. Phys. Lett.* **56**, 2530–2532 (1990).
- M. H. P. Pfeiffer, A. Kordts, V. Brasch, M. Zervas, M. Geiselmann, J. D. Jost, and T. J. Kippenberg, "Photonic damascene process for integrated high-Q microresonator based nonlinear photonics," *Optica* **3**, 20–25 (2016).
- Q. Li, A. A. Eftekhar, M. Sodagar, Z. Xia, A. H. Atabaki, and A. Adibi, "Vertical integration of high-Q silicon nitride microresonators into silicon-on-insulator platform," *Opt. Express* **21**, 18236–18248 (2013).
- N. Zen, T. A. Puurtinen, T. J. Isotalo, S. Chaudhuri, and I. J. Maasilta, "Engineering thermal conductance using a two-dimensional phononic crystal," *Nat. Commun.* **5**, 3435 (2014).
- Y. Liu, Y. Xuan, X. Xue, P.-H. Wang, S. Chen, A. J. Metcalf, J. Wang, D. E. Leaird, M. Qi, and A. M. Weiner, "Investigation of mode coupling in normal-dispersion silicon nitride microresonators for Kerr frequency comb generation," *Optica* **1**, 137–144 (2014).
- J. W. Coburn and H. F. Winters, "Plasma etching—a discussion of mechanisms," *J. Vac. Sci. Technol.* **16**, 391–403 (1979).
- C. J. Mogab, A. C. Adams, and D. L. Flamm, "Plasma etching of Si and SiO_2 —the effect of oxygen additions to CF_4 plasmas," *J. Appl. Phys.* **49**, 3796–3803 (1978).
- R. Pétri, P. Brault, O. Vatel, D. Henry, E. André, P. Dumas, and F. Salvan, "Silicon roughness induced by plasma etching," *J. Appl. Phys.* **75**, 7498–7506 (1994).
- X. Tang, V. Bayot, N. Reckinger, D. Flandre, J. P. Raskin, E. Dubois, and B. Nysten, "A simple method for measuring Si-F in sidewall roughness by AFM," *IEEE Trans. Nanotechnol.* **8**, 611–616 (2009).
- K. K. Lee, D. R. Lim, H.-C. Luan, A. Agarwal, J. Foresi, and L. C. Kimerling, "Effect of size and roughness on light transmission in a Si/SiO_2 waveguide: experiments and model," *Appl. Phys. Lett.* **77**, 1617–1619 (2000).
- M. Schaepkens, T. E. F. M. Standaert, N. R. Rueger, P. G. M. Sebel, G. S. Oehrlein, and J. M. Cook, "Study of the SiO_2 -to- Si_3N_4 etch selectivity mechanism in inductively coupled fluorocarbon plasmas and a

- comparison with the SiO₂-to-Si mechanism," *J. Vac. Sci. Technol. A* **17**, 26–37 (1999).
32. D. Beery, K. Reinhardt, P. B. Smith, J. Kelley, and A. Sivasothy, "Post etch residue removal: novel dry clean technology using densified fluid cleaning (DFC)," in *IEEE International Interconnect Technology Conference (Cat. No. 99EX247)* (1999), pp. 140–142.
 33. M. G. Blain, T. L. Meisenheimer, and J. E. Stevens, "Role of nitrogen in the downstream etching of silicon nitride," *J. Vac. Sci. Technol. A* **14**, 2151–2157 (1996).
 34. Y. Wang and L. Luo, "Ultrahigh-selectivity silicon nitride etch process using an inductively coupled plasma source," *J. Vac. Sci. Technol. A* **16**, 1582–1587 (1998).
 35. B. E. Little and S. T. Chu, "Estimating surface-roughness loss and output coupling in microdisk resonators," *Opt. Lett.* **21**, 1390–1392 (1996).
 36. F. Xia, L. Sekaric, and Y. Vlasov, "Ultracompact optical buffers on a silicon chip," *Nat. Photonics* **1**, 65–71 (2007).
 37. T. Tsuchizawa, K. Yamada, H. Fukuda, T. Watanabe, J. Takahashi, M. Takahashi, T. Shoji, E. Tamechika, S. Itabashi, and H. Morita, "Microphotonics devices based on silicon microfabrication technology," *IEEE J. Sel. Top. Quantum Electron.* **11**, 232–240 (2005).
 38. G. W. Reynolds and J. W. Taylor, "Factors contributing to sidewall roughness in a positive-tone, chemically amplified resist exposed by x-ray lithography," *J. Vac. Sci. Technol. B* **17**, 334–344 (1999).
 39. R. J. Bojko, J. Li, L. He, T. Baehr-Jones, M. Hochberg, and Y. Aida, "Electron beam lithography writing strategies for low loss, high confinement silicon optical waveguides," *J. Vac. Sci. Technol. B* **29**, 06F309 (2011).
 40. D. M. Tennant, R. Fullowan, H. Takemura, M. Isobe, and Y. Nakagawa, "Evaluation of a 100 kV thermal field emission electron-beam nanolithography system," *J. Vac. Sci. Technol. B* **18**, 3089–3094 (2000).
 41. X. Yi, Y.-F. Xiao, Y.-C. Liu, B.-B. Li, Y.-L. Chen, Y. Li, and Q. Gong, "Multiple-Rayleigh-scatterer-induced mode splitting in a high-Q whispering-gallery-mode microresonator," *Phys. Rev. A* **83**, 023803 (2011).
 42. M. L. Gorodetsky, A. D. Pryamikov, and V. S. Ilchenko, "Rayleigh scattering in high-Q microspheres," *J. Opt. Soc. Am. B* **17**, 1051–1057 (2000).
 43. D. S. Weiss, V. Sandoghdar, J. Hare, V. Lefèvre-Seguin, J.-M. Raimond, and S. Haroche, "Splitting of high-Q Mie modes induced by light back-scattering in silica microspheres," *Opt. Lett.* **20**, 1835–1837 (1995).
 44. K. Luke, A. Dutt, C. B. Poitras, and M. Lipson, "Overcoming Si₃N₄ film stress limitations for high quality factor ring resonators," *Opt. Express* **21**, 22829–22833 (2013).
 45. V. R. Almeida, R. R. Panepucci, and M. Lipson, "Nanotaper for compact mode conversion," *Opt. Lett.* **28**, 1302–1304 (2003).
 46. L.-W. Luo, G. S. Wiederhecker, J. Cardenas, C. Poitras, and M. Lipson, "High quality factor etchless silicon photonic ring resonators," *Opt. Express* **19**, 6284–6289 (2011).
 47. P. E. Barclay, K. Srinivasan, and O. Painter, "Nonlinear response of silicon photonic crystal microresonators excited via an integrated waveguide and fiber taper," *Opt. Express* **13**, 801–820 (2005).
 48. P. Rabiei, W. H. Steier, C. Zhang, and L. R. Dalton, "Polymer micro-ring filters and modulators," *J. Lightwave Technol.* **20**, 1968–1975 (2002).
 49. T. J. Kippenberg, S. M. Spillane, and K. J. Vahala, "Kerr-nonlinearity optical parametric oscillation in an ultrahigh-*Q* toroid microcavity," *Phys. Rev. Lett.* **93**, 083904 (2004).
 50. A. Matsko, A. Savchenkov, D. Strekalov, V. Ilchenko, and L. Maleki, "Optical hyperparametric oscillations in a whispering-gallery-mode resonator: threshold and phase diffusion," *Phys. Rev. A* **71**, 033804 (2005).
 51. K. Ikeda, R. E. Saperstein, N. Alic, and Y. Fainman, "Thermal and Kerr nonlinear properties of plasma-deposited silicon nitride/silicon dioxide waveguides," *Opt. Express* **16**, 12987–12994 (2008).
 52. H. Jung, C. Xiong, K. Y. Fong, X. Zhang, and H. X. Tang, "Optical frequency comb generation from aluminum nitride microring resonator," *Opt. Lett.* **38**, 2810–2813 (2013).
 53. B. J. M. Hausmann, I. Bulu, V. Venkataraman, P. Deotare, and M. Lončar, "Diamond nonlinear photonics," *Nat. Photonics* **8**, 369–374 (2014).
 54. M. Pu, L. Ottaviano, E. Semenova, and K. Yvind, "Efficient frequency comb generation in AlGaAs-on-insulator," *Optica* **3**, 823–826 (2016).
 55. A. A. Savchenkov, A. B. Matsko, D. Strekalov, M. Mohageg, V. S. Ilchenko, and L. Maleki, "Low threshold optical oscillations in a whispering gallery mode CaF₂ resonator," *Phys. Rev. Lett.* **93**, 243905 (2004).
 56. A. O'Keefe and D. A. G. Deacon, "Cavity ring-down optical spectrometer for absorption measurements using pulsed laser sources," *Rev. Sci. Instrum.* **59**, 2544–2551 (1988).
 57. D. Romanini, A. A. Kachanov, N. Sadeghi, and F. Stoeckel, "CW cavity ring down spectroscopy," *Chem. Phys. Lett.* **264**, 316–322 (1997).
 58. G. Berden, R. Peeters, and G. Meijer, "Cavity ring-down spectroscopy: experimental schemes and applications," *Int. Rev. Phys. Chem.* **19**, 565–607 (2000).
 59. T. Barwicz and H. A. Haus, "Three-dimensional analysis of scattering losses due to sidewall roughness in microphotonic waveguides," *J. Lightwave Technol.* **23**, 2719–2732 (2005).
 60. F. P. Payne and J. P. R. Lacey, "A theoretical analysis of scattering loss from planar optical waveguides," *Opt. Quantum Electron.* **26**, 977–986 (1994).